IEEE Access
Multidisciplinary | Rapid Review | Open Access Journal

Received January 4, 2021, accepted January 17, 2021, date of publication January 21, 2021, date of current version January 27, 2021.

*Digital Object Identifier 10.1109/ACCESS.2021.3053384*

# Functional Segmentation for Preoperative Liver Resection Based on Hepatic Vascular Networks

**DOAN CONG LE[1], JIRAPA CHANSANGRAT[2], NATTAWUT KEERATIBHARAT[3], AND PARAMATE HORKAEW[1]**

[1]School of Computer Engineering, Suranaree University of Technology, Nakhon Ratchasima 30000, Thailand
[2]School of Radiology, Suranaree University of Technology, Nakhon Ratchasima 30000, Thailand
[3]School of Surgery, Suranaree University of Technology, Nakhon Ratchasima 30000, Thailand

Corresponding author: Paramate Horkaew (phorkaew@sut.ac.th)

This work was supported in part by the Suranaree University of Technology, through SUT-Ph.D. Scholarship Program for Association of Southeast Asian Nations (ASEAN).

**ABSTRACT** Successful liver resection relies on accurate estimation of future liver remnant volume (FLRV). According to Couinaud's scheme, a liver is composed of eight functionally independent segments, each of which has its own vascular in- and out-flow tracks. Segmenting a liver by this scheme is vital to postoperative regeneration and hence prognosis outcome. Conventionally, estimation of liver segments was often done by hand on 3D computed tomography. The process is generally tedious, time consuming, and prone to observer variability. Alternatively, computerized methods had been proposed but impeded by anatomically irrelevant approximation and manually specified markers. To resolve the issues, this paper presents a novel method for functional liver segmentation. Its main contribution was performing analyses of differential geometry directly on a liver surface and interior venous system. Except for a few points being placed on major vessels, anatomical references required for defining all separating surfaces were automatically identified. To demonstrate its merits, virtual liver resection was implemented on the standard MICCAI SLIVER07 dataset, and the resultant segments were benchmarked against four most related works. Visual and numerical assessments reported herein indicated that our method could faithfully label all Couinaud's segments, especially the caudate, with lesser degree of user interaction. The preliminary findings suggested that it can be integrated into augmented surgical planning and intervention.

**INDEX TERMS** Computed tomography, Couinaud, differential geometry, hepatic vascular system, liver resection.

## I. INTRODUCTION

Liver resection has shown great outcomes in therapeutic intervention of various hepatic diseases. For example, patients suffered from hepatocellular carcinoma, mass-forming cholangiocarcinoma, and hepatic metastasis, have significantly improved prognosis, after underwent the procedure. Nonetheless, its success particularly depends on preoperative assessment of liver volume. When making surgical decision, care must be taken to ensure that remaining liver is adequate to maintain its normal function, otherwise the patient would be put at great risks of liver failure. A number of techniques have been proposed to determine postoperative liver sufficiency. In particular, future liver remnant volume (FLRV) can be estimated and employed as standardized determinant of postoperative outcome. Research by Kishi [1] and Abdalla [2] *et al.*, reported that this ratio correlates well with risks of liver failure, morbidity, and death. Resection has also been found operated on both donors and recipients in liver transplantation, for treating a patient with chronic liver diseases. In this surgical procedure, the size of a transplanted liver must fit to that of the recipient's body. As general criterion, the graft weight (GF) threshold must be 0.8-1.0% [3] of recipient's weight. On the other hand, postoperative complications are likely when the ratio exceeds 4.0% [4], [5], or falls below 0.8%. GF percentage is also applied in other contexts, e.g., preoperative portal vein embolization and post-transplantation assessment of graft regeneration, etc.

Traditionally, estimation of liver volume and functional segmentation were done manually on preoperative imaging, such as computed tomography (CT) [6]. Hand delineation of anatomical structure on medical images is tedious, time

The associate editor coordinating the review of this manuscript and approving it for publication was Carmen C. Y. Poon.

consuming, and prone to inter- and intra-observer variability [7]. Therefore, developing automated computer software to assist the maneuver could be beneficial in clinical usages.

Liver functions as an active filter by excreting wastes and toxin from oxygen and nutrition from the gastrointestinal circulatory system to the kidneys [8]. Contacting with excessive toxin carried via portal vein (PV) usually causes liver diseases, such as cirrhosis, fibrosis, and cancer. Unlike some other abdominal organs, a deteriorated liver cannot be substituted by any artificial prosthesis, but graft and regeneration of liver remnant. It is well received that a crucial part in successful clinical diagnosis, surgical planning, preoperative resection, and postoperative monitoring is played by understanding of subject specific functional structure of the liver and major hepatic vasculature.

As the standardized language among radiologists and surgeons, external shape of a liver is divided into two hemilivers, i.e., left, and right lobes, by hepatic vein (HV). Anatomically, Couinaud's work indicated that a liver comprises of eight functionally independent segments, each of which has its own vascular in- and out-flow, biliary drainage, and lymphatic drainage [9], [10]. With Couinaud's scheme, the subdivisions are based on the distribution of the two internal venous systems, i.e., three HVs and two PVs. Particularly, the right (RHV), middle (MHV) and left (LHV) hepatic veins divided a liver into the right posterior, right anterior, left medial and left lateral sections, respectively. These segments are further separated into interior and superior parts, by the left (LPV) and right (RPV) portal veins. Eight functional segments of a liver are labeled accordingly as follow: The anterosuperior and posteroinferior sectors of the right lobes which contain the segments V, VI, VII, and VIII are demarcated by RHV. This plane runs from inferior vena cava (IVC) to the gallbladder fossa, also called Cantlie's line. The falciform ligament separates the left lobe into media (the segment IV) and lateral parts (the segments II and III). Finally, the segment I, also referred to as caudate, is bounded posterior laterally by the fossa for the inferior vena cava, anteriorly by the ligamentum venosum, and inferiorly by porta hepatis.

Generally, functional comprehension and corresponding classification enable successful surgical procedures, such as accurate removal of only damaged section without causing risks to healthy ones. As such, with self-recovery, an operated liver may be able to regenerate within 3-12 months after a major resection surgery [11].

With the recent advances in computerized translational medicine, especially computer assisted diagnosis (CAD) and intervention (CAI), a number of methods were proposed to reduce time consuming and tedious traditional preoperative planning by means of anatomical models and virtual reality [12]–[15]. Thus far, existing techniques remained yet to be enhanced. Therefore, this paper proposes a novel method that is able to localize the hepatic vascular networks more accurately and efficiently, and to effectively delineate all functional segments (I-VIII) of a liver on its reconstructed 3D surface, prior to resection surgery. These are in order to better reduce adverse effects on patients and complications, thus extending their life expectancy.

The remainder of this paper is organized as follow: Section II surveys recent literature on major approaches to liver segmentations and annotations. Section III describes the proposed scheme, which was based on subject specific hepatic vascular network and by using differentiable geometry computing. The experimental results on a public dataset are reported and discussed in sections IV and V, respectively. Finally, section VI gives concluding remarks and future works.

## II. LITERATURE REVIEW

A liver, extracted from 3D tomography, may be described by either a set of binary interior voxels $\left(\mathbb{R}^3\right)$ or a 2-manifold $\left(\mathbb{R}^2\right)$ of enclosing ones. Accordingly, classifying its element into one of Couinaud's segments can be categorized, by these 3D descriptors, into those based on geometric functions on the respective domains, i.e., voxel and surface-based approaches. Reviews on the state-of-the-art liver functional segmentation are made in the next subsections.

### A. VOXEL-BASED APPROACH

With this approach, liver voxels are assigned to these segments based on the distances between their locations to a specific branch in the venous network. For example, Selle *et al.* [16], determined memberships of a segment, in reference to LPV and RPV. Therein, region growing was first applied to find a suitable threshold to extract the hepatic vascular network from the images. Thinning algorithm was then applied to skeletonize the extracted vessels, to define the network geometry, from which a vascular tree was created. After having HV removed from this tree using directed graph, a voxel was labeled by Laplacian (LSA) or nearest neighbor (NNSA) segment approximation. Nevertheless, computing the Laplacian on a voxel domain was intensive. A simpler and more straightforward method was proposed by Huang *et al.* [17], where both vessels and liver itself were projected onto planes. Firstly, three principal vectors were each defined by the intersection of the three major HV branches and the nearest point along the respective one. On labeling segments on both hemi-livers, two additional planes were each defined by separate normal vector. The one on the left plane was the average of the three principal vectors, while the right one was that of MHV and RHV. Evidently, vessel extraction was the key element in both methods. Yang, *et al.* [18] improved over Selle's one. In Yang's work, region growing was similarly applied to intensity images, but up to six Gaussian mixture models (GMM) were estimated. Among these GMM, the most suitable threshold interval was chosen to extract venous tree, whose major branches were then identified by using local searching. Couinaud segments of the liver were finally labeled following [16]. In addition to categorical search, Voronoi algorithm was adopted by Debarba [19] and Chen [20], *et al.*, to classify voxels

with their segments. Their difference was in calculating a Voronoi diagram. The first method used the distance from a voxel to seed points, handpicked on HV and PV, whereas the other considered only PV, when building eight vascular trees, from which distances to each voxel were measured. Zhang *et al.* [21], adopted similar strategy, but focused on enhancing vessel segmentations.

### B. SURFACE-BASED APPROACH

Unlike voxel-based ones, methods in this group classify hepatic segments directly on a reconstructed 3D liver surface, by various geometric elements, mostly ordinary planes. Similar to the previous approach, however, these elements were typically derived from main vascular branches. As one of a few exceptions, Boltcheva *et al.* [22] defined Couinaud's regions based on six landmarks, automatically detected on a liver, instead of its vascular network. Differential geometry was employed to detect two points on vena cava, two others on gallbladder bed, and two more points on inferior liver border of the left lobe. A total of five planes were constructed from these points and finally used to separate the liver volume. In other similar works, a liver was separated by using four [23] and three [24] planes. The former fitted the planes to three major HVs and PV, while the latter defined the planes from seven manually specified points on RHV, MHV, and LHV. In [24], superior and inferior regions were divided by another plane on an imaging slice, where PV was most visible. On this plane, caudate lobe (segment I) was also cut by a Bézier curve, whose four control points were manually defined by a user. Specifying these landmarks on a liver is, however, subjective, and dependent on user's experience. More consistent approach is to do so on salient features, e.g., those on main vascular networks. Provided skeletonized HVs and PV, but with their small branches removed, Lebre *et al.* [25] computed four corresponding directional vectors. The first three vectors originated from HV root and pointed along respective hepatic veins, within close proximity to their root. The last one was computed from the longest chain of vertical points along Z-axis. Liver subdividing planes were created from these vectors. Instead of cutting a liver by planes, some studies performed subdivision directly on an extracted liver surface into patches, corresponding to Couinaud's regions. For instance, Pamulapati *et al.* [26] first segmented hepatic vessels, from which undirected graph was then built, by using graph cuts and skeletonization, respectively. Vessel sections were labeled with either RHV, MHV, LHV, PV, or RPV, depending on their positions and orientations. Surface patches were traced from root to ends, via respective branching points in the subtrees. Much straightforward interactive method was proposed by Rusko *et al.* [27], where B-spline surfaces were interpolated from user defined control points on 2D slices. These control points were placed on the venous traces, provided that: 1) Each surface must be interpolated by at least three traces, each of which contained at least three points. 2) There was no self-intersection in any trace. 3) The view on which a trace was drawn must be consistent, i.e., either axial, coronal, or sagittal. In 2020, the most recent study by Alirr and Rahni [28], connected the vena cava with HV centerlines, defined on individual slices, to build three hepatic planes, while the portal plane was defined by a selected image slice. Therein, the veins bifurcations were located by deforming statistically trained atlas to match extracted vasculature on CT images.

### C. SUMMARY OF LATEST ALGORITHMS

Some remarks may be drawn from the above surveys. The methods in the former group [16]–[21] partitioned a liver based on membership values associated with interior voxels. Thus, their major hinderance was evaluation of membership function for each voxel with respect to relevant features, such as vascular structures, was computationally intensive. In addition, no topological violation of any resulted segment was asserted either on individual voxels or their aggregation. Nor did they consider exterior anatomical landmarks, such as falciform ligament and gallbladder fossa, or liver appearance in general [16]. Although Zhang *et al.* [21] specifically followed Couinaud's theory, but their empirical assumptions on vasculature were not adequate to completely avoid post-process correction by an expert. With much less data involved, when only extracted liver surface and vascular outlines were considered, even greater user interaction was inevitable for methods in the second group [22]–[27]. Take Butdee's and Rusko's method [24], [27] for examples. Segmenting required at least ten user defined points, and at least three traces, each with at least three points, for creating sectional planes and B-spline surfaces, respectively. These subjective processes caused not only fatigue during batch analyses, but also significant observer variability. A deformable statistical atlas [28] could help elevating manual intervention, provided that sufficiently large training set was available. Unlike other methods in its group, the one, suggested by Boltcheva *et al.* [22], relied solely on the shape of liver, while neglecting its interior vasculature. Lastly, most of works in both groups, except [20]–[22], [24], did not report any annotation of caudate lobe (segment I).

## III. PROPOSED METHOD

To remedy these issues, this paper proposes an integration of salient features of a liver surface and concise representation of its vascular networks, both automatically reconstructed from 3D CT. This information was incorporated, as functional definitions and constraints, into segmenting a liver, strictly according to Couinaud's scheme. Compared to the works previously discussed, our method was able to completely label all eight functional segments, including caudate, at greater precision, but with minimal user interaction involved.

Overview of the proposed scheme is depicted in Fig. 1. Given volumetric CT images of a 3D liver scan, the liver and interior vasculature were first extracted automatically by using a CAD software written in our laboratory, based on off-the-shelf algorithms. Next, centerlines traversing through

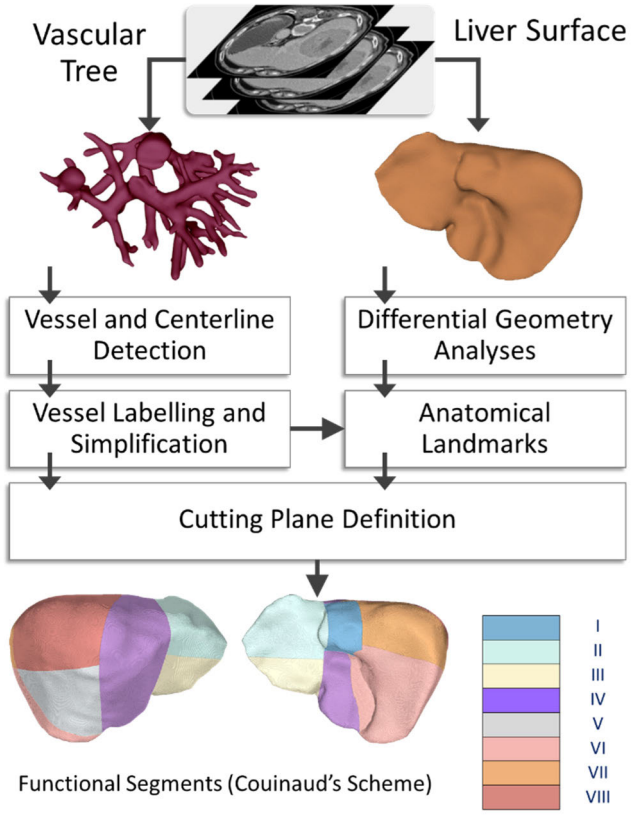


**FIGURE 1.** Diagram showing the key steps in the proposed functional liver segmenting scheme.

the vascular networks were reconstructed, while differential geometric properties were computed on the extracted liver surface, simultaneously. Subsequently, the surface properties would be analyses and used to characterize key anatomical landmarks, i.e., gallbladder fossa and inferior ridge sections. Later, a set of cutting planes were defined, based on vascular passages and landmarks. Finally, functional Couinaud's segments of the liver (I–VIII) were determined, by means of combinatorial operations on the liver surface and geometric descriptors.

### A. LIVER AND VESSELS SEGMENTATION

Segmenting a liver and its interior vascular network from volumetric CT is a challenging task due to inhomogeneous intensity and ambiguous boundaries in some areas. Several methods have been proposed in the literature [29], [30]. However, since their detailed treatment and analyses fell out of scope of this paper, we adopted generic yet efficient off-the-shelf algorithms and implemented in-house software to perform these tasks. Firstly, multivariate mixture models [31], was applied to these CT images, to assign an individual voxel to abdominal tissue, vessel, and background classes, with associated probabilities. Subsequently, to enhance the fidelity of multi-class labelling, relaxation labeling (RL) was performed to regularize the initial probabilities, based on contextual information [32]. Graph cut [33] algorithm was then used to extract the liver and enclosed vessels, based on their spatial relationship. The corresponding 3D surface meshes were finally reconstructed by the Marching Cubes [34] and later used as inputs to the subsequent steps in the proposed segmentation pipeline.

### B. TRACING VASCULAR CENTERLINES

Referring parts of a liver to respective functional segments required not only its morphological cue but also accurate localization and measurement of enclosed vascular branches. To this end, skeletonization was a viable tool for consolidating voxelate data, while maintaining precise geometry and valid topology of the underlying network. Therefore, in this work, a method proposed by Antiga *et al.*, [35] was adopted. Once skeletonized, all but major branches were trimmed off, based on their regional radii. Subsequently, a user was asked to specify the starting and end points of the HV and PV. Generally, the former was located at the root, while the latter was at the first bifurcation point toward the end of a respective vein, as illustrated in Fig. 2. It is worth noted that since their definitions were quite explicit, the criteria could be embedded in a computer program and hence having the markers specified automatically. That said, detailed implementation fell out of scope of this study but may be found elsewhere [21], [30]. Apart from this minimal intervention, the remaining of segmentation process was fully automatic.

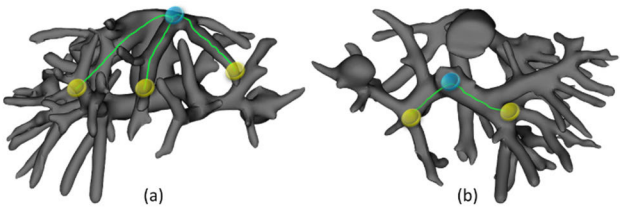


**FIGURE 2.** The extracted venous system with overlaid centerlines. Seven manually specified stating (blue) and end (yellow) points on HV and PV are shown in an interior (a) and posterior views (b), respectively.

Given the extracted centerlines and respective markers on the primary venous system, their approximating vectors were next determined by principal component analysis (PCA) [36] of all points within the corresponding vascular section.

### C. FUNCTIONAL SEGMENTATION

Unlike existing methods, a main contribution of the proposed scheme is that, from this step onward, virtual resection was performed directly and automatically, by referring only to the specified interior vascular markers and differential geometries evaluated on the surface. This process was divided into five modules, whose details are explained as follow:

#### 1) DIFFERENTIAL GEOMETRY OF THE FEATURES

While other studies relied the separations of anterior from posterior segments and of left from right lobes on some approximating planes that were either inferred from distance functions and additional markers, or manually defined, the proposed method aimed at detecting discernible

anatomical features, which were gallbladder fossa and inferior ridge. Topologically, the gallbladder fossa appears as a narrow surface that spreads from the top of falciform ligament to the bottom of gallbladder area. The inferior ridge lies at the bottom of the liver, and extends from left to right lobe, passing under gallbladder fossa. Geometrically, the former may be characterized by the most concave partial surface on the posterior liver. Likewise, the latter corresponds to the most convex path along the inferior fringe. These features were identified accordingly by mean curvature expression, described as follow:

Let $\psi$ be a 2-manifold embedded on 3D Euclidean space, and $d\psi$ be its derivative, locally defined at a point, $\boldsymbol{p}$, by an infinitesimal plane, whose tangent and normal along the direction $\theta \in [0, 2\pi]$, are defined by unit vectors, $X_\theta$ and $n$, respectively. The plane curvature, denoted by $k(\mathbb{P})_\theta$, is then measured by that of the curve, formed by intersection between $\psi$ and $d\psi$. The mean of these curvature is therefore an average over all directional curvatures [37], i.e.

$$k(\mathbb{P}) = \frac{\int_0^{2\pi} k(\mathbb{P})_\theta d\theta}{2\pi} \tag{1}$$

Euler's theorem stated that the mean curvature can also be computed by an average of principal curvatures, i.e.,

$$k(\boldsymbol{p}) = \frac{k(\mathbb{P})_{\theta_1} + k(\mathbb{P})_{\theta_2}}{2} \tag{2}$$

where the principal curvatures, $k(.)_{\theta 1}, k(.)_{\theta 2}$, are the maximum and minimum curvatures, evaluated at specific location and corresponding to directions, $\theta_1$ and $\theta_2$, respectively.

The mean curvature is one of the most important intrinsic properties of a surface and is invariant to geometric transformation. It has been utilized in a range of applications, from computational science, medicine, and engineering [38]–[40]. In this study, it was evaluated on discrete triangular mesh of the extracted liver [41], [42] and then employed as a determinant for anatomical feature classification.

Let $\boldsymbol{V} = \{v_1, v_2, \ldots, v_N | v_i \in \mathbb{R}^3, 0 \le i \le N\}$, be a set of $N$ vertices constituting a whole liver surface, and $k(v_i)$ be the mean curvature at a vertex $v_i$. Assume further that the distribution of these curvatures over the surface is Gaussian, with mean and standard deviation (SD), $\mu_k$ and $\sigma_k$, respectively. Example of typical mean curvature distribution overlaid on a liver surface is shown in Fig. 3a and 3b.

Firstly, to determine gallbladder fossa, let $\boldsymbol{V}_c \subset \boldsymbol{V}$, be a set of concave vertices, whose mean curvatures are lower than a threshold, given by a real positive constant $a$, and the Gaussian parameters, i.e.,

$$\boldsymbol{V}_c(a) = \{v \in V | k(v) \le \mu_k + a * \sigma_k\} \tag{3}$$

A concave set satisfying the above criterion (rendered in red) may consist of multiple connected regions (patches), each of which is denoted by $\boldsymbol{v}_j$, i.e., $\boldsymbol{V}_c(a) = \bigcup_j \boldsymbol{v}_j$. As it appears in Fig. 3b, the gallbladder fossa is a narrow and highly concave strip, located approximately between left and

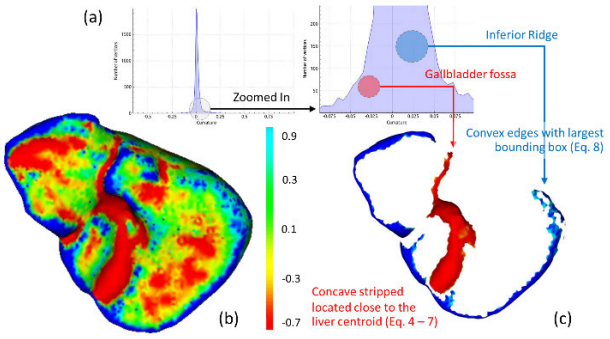


**FIGURE 3.** An example of mean curvature distribution (a) on a liver surface (b), the corresponding extraction (c) of gallbladder fossa (red) and inferior ridge (blue) based on the thresholding and those based on anatomical criteria.

right lobes. The geometrical appearance of a $j^{\text{th}}$ patch $\boldsymbol{v}_j$ is characterized by a function of its normalized width and curvature, that is,

$$E(\boldsymbol{v}_j) = \frac{1}{\|L_j\|} \bullet \frac{|V|}{|\boldsymbol{v}_j|} \sum_{v \in \boldsymbol{v}_j} d_\perp(v, L_j) \cdot e^{-\left(\frac{k(v)}{\sigma_k}\right)^2} \tag{4}$$

where $L_\text{j}$ and $||L_\text{j}||$ are the principal axis passing through the centroid of $\boldsymbol{v}_j$, and its length, respectively. The norms, $|\boldsymbol{V}|$ and $|\boldsymbol{v}_j|$ are the numbers of total vertices and those of the $j^{\text{th}}$ connected patch, respectively. In addition, the distance function $d_\perp(p, L)$ is the shortest distance from a point $p$ to a line $L$. The lower the $E$ value, the more likely the patch is of gallbladder fossa. To further ensure accurate identification of the structure, additional location constraint was imposed on its centroid being closest to that of the whole liver, that is,

$$d(\bar{\boldsymbol{v}}_j, \bar{\boldsymbol{V}}) = \|\bar{\boldsymbol{v}}_j - \bar{\boldsymbol{V}}\|_2 \tag{5}$$

where $\bar{\boldsymbol{v}}_j$ and , $\bar{\boldsymbol{V}}$ are centroids of the respective surfaces and $d(\cdot, \cdot)$ is a Euclidean distance between two points.

For given $a$ and hence $\boldsymbol{V}_c(a)$ in Eq. (3), the surface patch, $j^{\text{th}}$ that has both the lowest $E(\boldsymbol{v}_j)$ and $d(\bar{\boldsymbol{v}}_j, \bar{\boldsymbol{V}})$ was chosen as a candidate. A grid search was run for $a \in [-0.5, 0]$. And once completed, the best candidate, whose costs were the lowest, was identified. Particularly, if $\boldsymbol{v}_j \subset \boldsymbol{V}_c(a_j)$ and $\boldsymbol{v}_i \subset \boldsymbol{V}_c(a_i)$ be the running candidates found at rounds $j$ and $i$, with constants, $a_j$ and $a_i$, respectively, then a patch $\boldsymbol{v}_j$ would be identified as gallbladder fossa, denoted by $\boldsymbol{v}_\text{gal}$, only if, for $i \ne j$, they simultaneously satisfied the following conditions:

$$E(\boldsymbol{v}_j) < E(\boldsymbol{v}_i) \tag{6}$$

$$d(\bar{\boldsymbol{v}}_j, \bar{\boldsymbol{V}}) < d(\bar{\boldsymbol{v}}_i, \bar{\boldsymbol{V}}) \tag{7}$$

Secondly, the inferior ridge (rendered in blue), denoted by $\boldsymbol{v}_\text{ird}$, is simply defined as all connected regions, that are more convex than a specified threshold, given by a real positive constant $b$ and the Gaussian parameters, i.e.,

$$\boldsymbol{V}_x(b) = \{v \in V | k(v) \ge \mu_k + b * \sigma_k\} \tag{8}$$

Unlike $\boldsymbol{v}_\text{gal}$ that is defined as a singly connected region, $\boldsymbol{v}_\text{ird}$, is all the regions, $\boldsymbol{v}_k$, that satisfy Eq. (8), that is, $\boldsymbol{V}_x = \bigcup_k \boldsymbol{v}_k$.

However, similar to identifying gallbladder fossa, an optimal value of $b$ and hence respective set $\boldsymbol{V}_x(b)$ were determined for $b \in [0, 0.5]$, by grid searching. In this case, the best candidate for the inferior ridge was that with the least number of vertices but the largest bounding box.

In our preliminary trials, it was found that the optimal constants, $a$ and $b$ in Eq. (3) and (8), in a shape instance as shown in Fig. 3c, were –0.3 and +0.3 (∼38.21% at both ends), respectively. Likewise, the constants were computed automatically for the remaining of the dataset.

### 2) LOCATING PRIMARY FUNCTIONAL LANDMARKS

Once the gallbladder fossa ($\boldsymbol{v}_{\text{gal}}$) and inferior ridge ($\boldsymbol{v}_{\text{ird}}$) were extracted from the liver surface, these cloud points were skeletonized by using global center technique [43]. The resulted curves, i.e., $\boldsymbol{C}_{\text{gal}}$ and $\boldsymbol{C}_{\text{ird}}$, respectively, consisted of ordered vertices, outlining the anatomical features, shown in Fig. 4a.

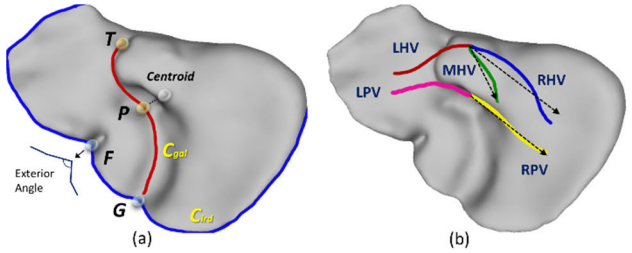


**FIGURE 4.** Examples of four functional landmarks on gallbladder fossa (T, P) and inferior ridge curves (G, F) (a), and three principal vectors, approximating MHV, RHV, and RPV (b).

A falciform ligament marker, denoted by a point $\boldsymbol{T}$, was first placed at the tip of $\boldsymbol{C}_{\text{gal}}$. Then, the entry point to the main PV, denoted by a point $\boldsymbol{P}$, was placed on the same curve, but closest to the liver centroid. The latter, identified as hepatic hilum, featured as an inferior margin of the caudate segment. On the $\boldsymbol{C}_{\text{ird}}$ curve, a corner point $\boldsymbol{G}$ was placed closest to the bottom end of the $\boldsymbol{C}_{\text{gal}}$. Finally, a point $\mathbf{F}$ was defined as the one that lied within a spherical neighbor of radius $\mathbb{h}$ to $\boldsymbol{G}$ and with minimal exterior angle. Anatomically, it was located on the same side as $\boldsymbol{T}$ and at the fissure on inferior surface between right and left lobes. The points $\boldsymbol{T}$ and $\boldsymbol{F}$ marked both ends of falciform ligaments that attaches the liver to the front body wall and acts like a natural plane separating the left lobe into medial and lateral sections [44], [45].

### 3) LABELING VESSELS AND EXTRACTING THEIR PRINCIPAL VECTORS

Subsequently, the primary landmarks located in the previous module were used to label five major branches from the vascular network, extracted earlier. They were LHV, MHV, RHV, LPV and RPV. To this end, first let $p^S_{HV}$ and $p^S_{PV}$ be the starting points of hepatic and portal veins, respectively. In addition, let $d(\boldsymbol{P}, p^S_{HV})$ and $d(\boldsymbol{P}, p^S_{PV})$ be their Euclidean distances to the entry point of main portal vein, $\boldsymbol{P}$. Then, the HV and PV could be distinguished by their distances to this entry point, that is, $d\left(\boldsymbol{P}, p^S_{HV}\right) > d\left(\boldsymbol{P}, p^S_{PV}\right)$. Likewise, three and two branches of HV and PV could be labeled according to relative distances from their midpoints to the falciform ligament markers, $\boldsymbol{T}$ and $\boldsymbol{F}$, following to Eq. (9) and (10), respectively.

$$d\left(\boldsymbol{T}, \bar{\boldsymbol{C}}_{LHV}\right) < d\left(\boldsymbol{T}, \bar{\boldsymbol{C}}_{MHV}\right) < d\left(\boldsymbol{T}, \bar{\boldsymbol{C}}_{RHV}\right) \quad (9)$$

$$d\left(\boldsymbol{F}, \bar{\boldsymbol{C}}_{LPV}\right) < d\left(\boldsymbol{F}, \bar{\boldsymbol{C}}_{MPV}\right) \quad (10)$$

where $\bar{\boldsymbol{C}}_V$ were the center points of a respective vein, $V$, i.e., LHV, MHV, RHV, LPV, and MPV.

Vascular geometries markedly differ across subjects but conformed to gross anatomy of the organ [21]. Therefore, to ensure adaption to these variations, while maintaining gradual surface resection trajectory, and hence realistic preoperative simulation, these hepatic and portal branches were simplified by approximating vectors. Unfortunately, due to dissensions in the literature regarding characterization of the lateral segments, only MHV, RHV, and RPV were thus approximated, by using generic PCA, as illustrated in Fig. 4b. This statistical operation is useful in spanning orthogonal bases that best describes underlying data points with respect to their spatial variances. That being said, unlike other resection methods, there was no cutting hyperplane reconstructed at this stage as yet, due to limited degrees of freedoms (DOF) of the vessels and their incurvate paths. Instead, in this paper, these principal vectors, each of which approximated a major branch, were jointly considered with the previously labeled landmarks to better and more robustly determine the resection planes.

### 4) DETERMINING THE RESECTIONS PLANES

One of the most crucial modules is determining the planes that separate the liver volumetry into functional segments according to Couinaud's classification. This module began with constructing three vertical planes, namely, $\Pi_{MHV}$, $\Pi_{RHV}$, and $\Pi_{LHV}$. These planes divided a liver into posterior, anterior, medial, and lateral sections. Unlike the other sections, the lateral one was a part of the left lobe and was separated by falciform ligament. Both LHV and falciform ligament were thus used to create the left ventricular plane ($\Pi_{LHV}$). Subsequently, the left and right horizontal planes, namely $\Pi_{RPV}$ and $\Pi_{LPV}$, were used to separate the inferior from superior parts. Examples of these planes are illustrated in Fig. 5.

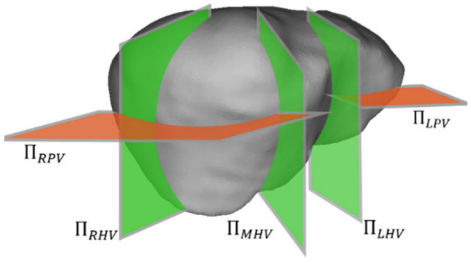


**FIGURE 5.** Illustration of three vertical and two horizontal planes, initially defined on a liver surface.

**TABLE 1. Expressions of MHV, RHV, and RPV planes.**

| Plane | Expression | Remark |
|---|---|---|
| MHV | $\Pi^t_{MHV}\left(\vec{h}_{MHV}, \boldsymbol{G}\right)$ | |
| RHV | $\Pi^t_{RHV}\left(\vec{h}_{RHV}, \boldsymbol{G}\right)$ | |
| RPV | $\Pi^t_{LHV}\left(\vec{h}_{TF}, \boldsymbol{q}\right)$ | Planar approximation of falciform ligament. |

Assume that a resection plane is defined, either by orthogonal $\Pi^n\left(\vec{n}_{(.)}, p\right)$ or tangent $\Pi^t\left(\vec{h}_{(.)}, p\right)$ expressions. The former is a plane, defined by a normal vector $\vec{n}$ and a point $p$, while the latter is that containing both tangential vector $\vec{h}$ and point $p$.

Firstly, let $\vec{h}_{MHV}$, $\vec{h}_{RHV}$, and $\vec{h}_{RPV}$ be the principal vectors, corresponding to MHV, RHV, and RPV, respectively. Let $\vec{h}_{TF}$ be the vector pointing from point $\boldsymbol{T}$ toward $\boldsymbol{F}$, along the falciform ligament. Accordingly, the vertical planes, defined by these veins are expressed in Table 1.

where $\boldsymbol{q}$ is an arbitrary point on LHV, chosen so that the area of a 3D closed curve formed by intersection between $\Pi_{LHV}$ and liver volume is minimized.

Secondly, for the horizontal planes, let $\vec{n}_{MHV}$ and $\vec{n}_{RHV}$ be the normal vectors of MHV and RHV planes, respectively, $\vec{n}_{RPV}$ be a normal vector perpendicular to a plane defined by $\vec{h}_{RPV}$ and an average between let $\vec{n}_{MHV}$ and $\vec{n}_{RHV}$, and also, $\boldsymbol{r}$ be a point on $\vec{h}_{RPV}$. Accordingly, the RPV plane is expressed by $\Pi^n_{RPV}\left(\vec{n}_{RPV}, \boldsymbol{r}\right)$. Finally, the LPV plane, $\Pi_{LPV}$, was defined such that it was initially perpendicular to $\Pi_{LHV}$ and then rotated iteratively about $\vec{n}_{LHV}$ axis, until it was also normal to a principal plane ($\Pi_P$), in which projections of points on the left branch of PV had greatest variance (well distributed).

Another contribution of this paper is accurate labeling of caudate segment, separated from left and right lobes, by anatomical boundaries. Oxygenated and nutrient blood flow enters this segment via PV, before directly draining into IVC. Accurate localization of the segment plays a crucial role in diagnosing and surgical intervention of hepatic diseases [46], particularly, Hepatocellular carcinoma (HCC) [47].

Nonetheless, computer assisted extraction of caudate segment from nearby sections remained problematic, because of its morphological variants and ambiguous boundaries, especially on CT images. However, a radiologist could identify caudate segment by its general appearance, i.e., rectangle, piriform or irregular form [48]. From posterior perspective, it is positioned behind the hepatic helium and in front of LPV. Its upper end is bounded by HV. To its left is ligamentum venosum, whereas its right margin is unclear [47]–[50]. As a result, this structure had so far been disregarded by most CAD studies. To reiterate the survey on this issue, Cheng *et al.* [20] adopted Sell's NNSA technique [16] and labeled caudate voxels, while Boltcheva [22] located this segment by extending MHV and RHV planes, and hence extrapolating their intersections with the liver. Lastly, Butdee *et al.* [24] interpolated the structure by manually delineated Bézier curves. Implying caudate segment solely by geometrical elements, these techniques discarded its morphological contexts as well as surrounding vascular and other hepatic structures, and hence were not sufficiently accurate.

It was suggested in [50], that IVC can be considered as the right margin of caudate segment. Unfortunately, IVC is not always discernable on CT images nor on a liver surface. With the proposed method, IVC was hence approximated by a line. It was observed that IVC is almost parallel to falciform ligament, which is commonly characterized by concave region in the middle of the liver surface (C.2). Therefore, to simplify the IVC, it was defined by a segment $\boldsymbol{AP}$, as shown in Fig. 6.

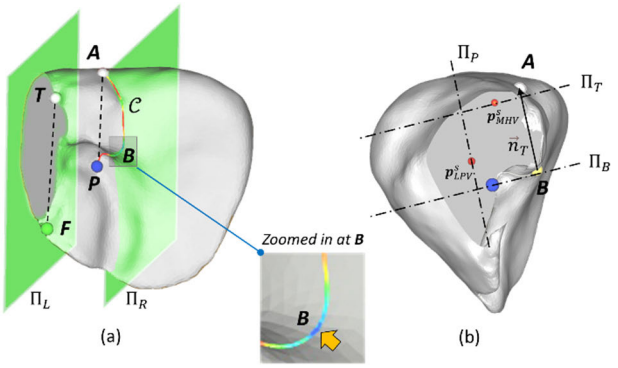


**FIGURE 6. Configuration of five bounding planes and a surface of the caudate segment. Figures (a) depicts left and right planes, while (b) depicts and top, bottom, and posterior planes, respectively.**

In this figure, $\boldsymbol{P}$ was the entry point to the main portal vein (C.3), while $\boldsymbol{A}$ is an intersection between the liver and a line passing $\boldsymbol{P}$ and parallel to $\vec{h}_{TF}$ (C.4). Then, the caudate segment is that bounded by the liver exterior and the following planes, as listed in Table 2.

To define the top plane, assuming $C$ be a curve segment that was formed by the intersection between the liver surface and bounded by points $\boldsymbol{P}$ and $\boldsymbol{A}$. Then, $\boldsymbol{B}$ was a point on this curve that had the highest curvature. The normal vector and point associated with the top plane was $\vec{n}_T = A - B$, and the starting point of MHV, $\boldsymbol{p}^s_{MHV}$, respectively. Similarly, the posterior plane was defined by an orthogonal vector $\vec{n}_P = \vec{n}_T \times \vec{n}_{LHV}$ and the starting point of LPV, $\boldsymbol{p}^s_{LPV}$.

Finally, provided these planes were defined as such, resections of all eight functional segments as per Couinaud's scheme could be performed virtually by tracing along their intersecting curves with the extracted liver surface.

## IV. EXPERIMENTS

This section presents experimental process on public dataset, functional liver resections, validations and benchmarking, and relevant discussions. However, while visual assessment was straightforward, due to thorough documented liver anatomy, numerical comparison was not quite the case. This was primarily because there have not been

**TABLE 2. Expressions of the bounding planes and surface of the caudate segment.**

| Plane | Expression | Remark |
|---|---|---|
| Left | $\Pi_L^t(\vec{h}_{MHV}, \boldsymbol{G})$ | See section (C.4) for $\Pi_{LHV}^t$ |
| Right | $\Pi_R^n(\vec{n}_{LHV}, \boldsymbol{P})$ | |
| Top | $\Pi_T^n(\vec{n}_T, \boldsymbol{p}_{MHV}^s)$ | See text and Fig. 6 for $\vec{n}_T$. |
| Bottom | $\Pi_B^n(\vec{n}_T, \boldsymbol{P})$ | |
| Posterior | $\Pi_P^n(\vec{n}_P, \boldsymbol{p}_{LPV}^s)$ | See text and Fig. 6 for $\vec{n}_P$. |
| Anterior | Liver surface | Exterior surface of the liver |

many studies, presenting entire functional liver segmentation, and there were even fewer, validating on the common datasets. Take for instance, Oliveira *et al.* [23] demonstrated their method on 7 CT images. In that work, the method was evaluated for consistency of a specialist's perception. Similarly, Boltcheva *et al.* [22] analyzed 7 images but of a different dataset and measured the errors between the resultant resection planes and those defined by experts. Pamulapati *et al.* [26] studied 13 CT images. In their experiments, 20 points were randomly placed inside a liver, within 2 cm. from its edge. Their (automatically) labeled segments were validated against those identified by a radiologist. There were few studies analyzing standard references. Rusko *et al.* [27], for example, used 14 out of total 20 CT images from MICCAI dataset. Their method was validated by comparing averaged volume of each segment from three test runs against those reported in the literature. Other works [21], [25], [28] employed some samples from public liver images, but lacking ground truth for functional segments has led to direct comparison being problematic.

To elevate standardize issues, a benchmarking framework was designed, in this study. Firstly, segmented livers were assessed visually, by an experienced radiologist. Objective evaluations were made by measuring and comparing relative hepatic sub-volumes, at three different levels, i.e., lobes (left and right), sections (lateral, medial, anterior, and posterior), and functional segments (I-VIII), respectively.

### A. LIVER DATASET

The recent needs for common ground truth for validating liver segmentation, and particularly the grand challenges called for MICCAI SLIVER07 initiative [51]. This study analyzed this MICCAI dataset, which consisted of 20 volumetric CT images, acquired at the resolution of 512 × 512 pixels by machines with 4, 16, and 64 detectors. Each volume consisted of 64 to 394 slices. Since these data were intended for general purposes liver analyses, and due to limited visibility of the vascular networks in some subjects, they were hence discarded. Accordingly, only 12 out of 20 volumes were considered in the subsequent experiments. Apart from that of liver volume, ground truth of neither its vessels nor functional segment annotations was available. Another liver database worth mentioned here is 3DIRCADb [52]. This CT database contains abdominal images of the same resolution as SLIVER07. It includes not only liver contours, but also vascular and tumor annotations. Nonetheless, 3DIRCADb does not specifically provided any references for Couinaud's segments. In a few instances, their locations were partially inferred from those of tumors, when and only if present. These inferences were exploited in [25], where diseased segments in few volumes (i.e., 5 out of 20) could be validated. To the best of our knowledge, there has yet no quantitative report on Couinaud's segmentation from 3DIRCADb images, against which we could compare our results. Moreover, to ensure robustness of the proposed algorithm, hepatic vasculature extracted (II, A. and B.) were firstly approximated by principal vectors (III, C.3), which were then mutually considered with anatomical landmarks, to estimate liver resection planes. Consequently, detailed information on these vessels, especially at smaller scale, were not imperative. In the following experiments, SLIVER07 data were thus acceptable.

### B. SYSTEM ENVIRONMENT AND SETTINGS

This study used open-source libraries, called Visualization Toolkit (VTK) [53] and Vascular Modeling Toolkit (VMTK) [54]. The first library has been widely used in many medical imaging studies, thanks to its ability to parse standard DICOM image and its meta data. It also allows intuitive graphical manipulations of a 3D object, e.g., geometrical operations, material processing, representing a model in points, wireframes, or surfaces forms, slicing, and clipping, etc. The VMTK was typically used to perform 3D vascular segmentation, centerline detection, mesh generation, and geometrical analyses. Due to their cross-platform implementation, all of the remaining processes were written in C/ C++ and Python languages and compiled to Linux x86 architecture. The implemented software was executed on a laptop personal computer (PC) of moderate specifications. It was equipped with an Intel©CPU clocked at 2.4 GHz, and 8 GB DDR3 RAM.

## V. RESULTS AND DISCUSSIONS

This section reports both visual and numerical assessment, of the proposed automated Couinaud's functional segmentation. Critical comparisons against state-of-the-art methods and critical discussion on the findings were also given.

### A. VISUAL ASSESSMENT

To ensure functional independence among eight segments and thus rapid recovery, for instance, after graft transplant, a liver should be resected into segments, each of which has sufficient inflow and outflow blood passages. Since not only interior venous network, but also differential surface exterior, were considered, the resection paths appear natural, yet attuned well to the overall shape and anatomical landmarks, as shown in Fig. 7. As also clearly noticed on axial and sagittal views, each segment has at least a pair of in- and out flows. Furthermore, the smallest caudate segment was

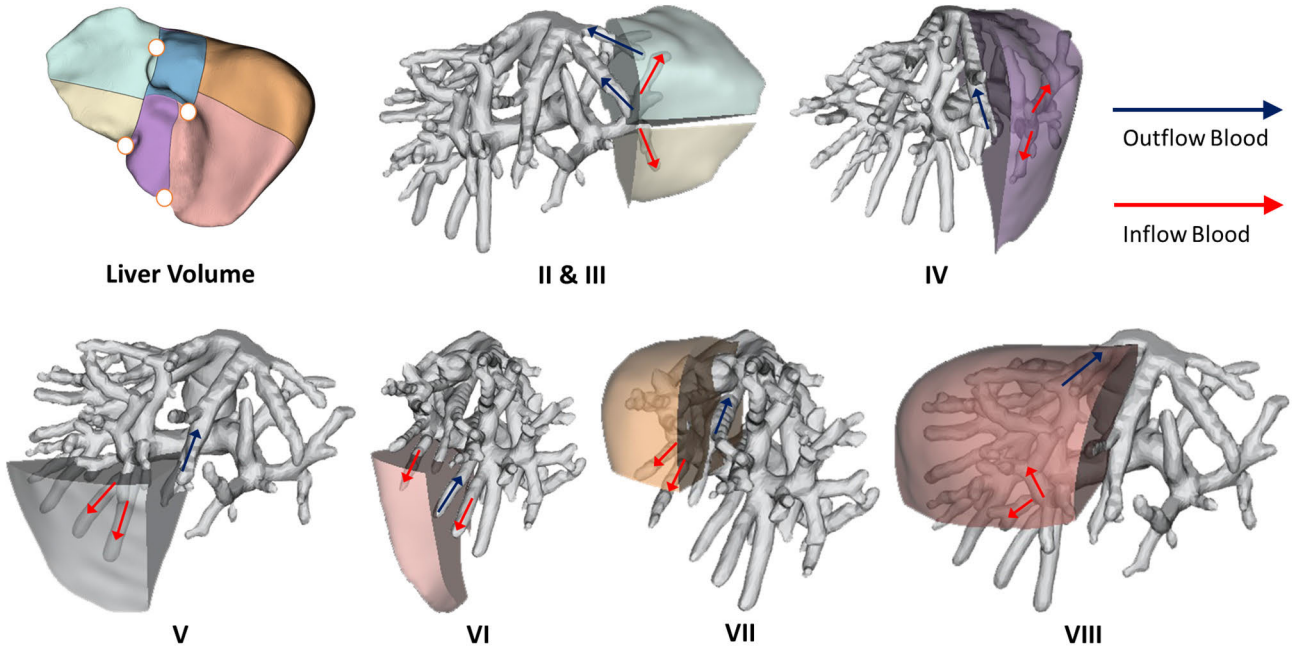


**FIGURE 7.** Example of the distribution of in- and out blood flows within each functional segment.

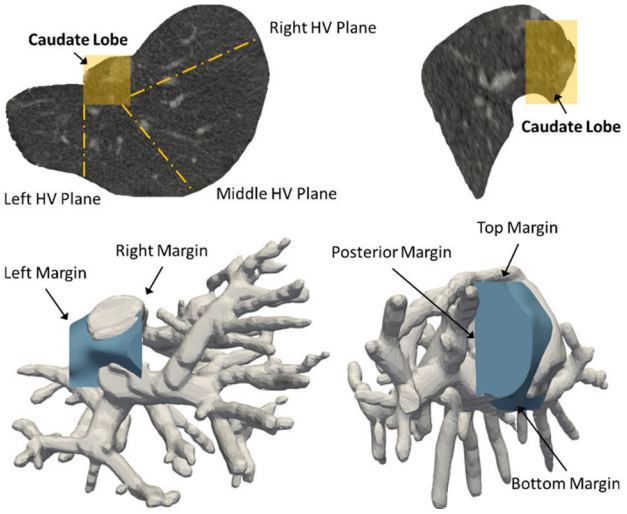


**FIGURE 8.** Localization of a caudate segment in 2D (top row) and 3D (bottom row) on axial (left column) and sagittal views (right column), showing the natural anatomical margins.

correctly localized by HV, IVC, entrances to MHV and PV, and LPV, as shown in Fig. 8.

### *B. NUMERICAL ASSESSMENT*

In addition to sufficient blood flows, there are other factors that determine the likelihood of postoperative recovery, such as minimal volume of FLRV, patient's age, their diabetes conditions, chemotherapy associated injury, blood loss during surgical procedure, and cholestasis, etc.

Among these determinants, FLRV is generally accepted as the most prevailing for postoperative outcome [55]. Therefore, to increase patient's survival rate, this factor must be meticulously observed when planning a liver surgery. For example, to ensure regeneration capacity of a liver after tumor removal, the average FLRV is 25% (15-40%) of a total liver volume. This ratio increases up to 50% (25-90%) in cirrhotic, depending on the stage of the disease and patient's age. For transplant surgery, minimal FLRV for the living donor is 40% on average (30-50%), while the accepted graft per recipient's weight ratio is 0.8% (0.8-1.0% [3] or, as indicated in more recent studies, 0.6-1.2% [56]–[58]).

It may be concluded that accurate calculation of relative liver volume as well as localization of its segments are critical for resection planning. Nevertheless, due to lack of common ground truth, and approximation of major vascular vectors, instead of dice similarity coefficient (DSC) or volume overlap error (VOE), this study introduced multi-level quantification, based on percentage of segmented volumes over total liver. By this approach, we were able to validate our resultant functional segments, against those obtained by four related methods, proposed in the literature. It is hypothesized that any misclassified (or contradicted) areas would manifest not only in anatomical violation, but also in adjacent partial volume deviation from its general cluster, at corresponding hierarchical levels.

#### 1) OVERVIEW OF FUNCTIONAL SEGMENTS

Unlike other whole liver extraction studies, where focused was placed on its shape boundaries, 12 out of 20 subjects were selected from the SLIVER07 dataset, based on the clarity of vessel appearance. Volumes of all annotated functional segments per subject are listed in Table 3 and summarized in Fig. 9.

Since the liver volumes were subject specific, and hence varied in both size and shape, their percentage values, relative

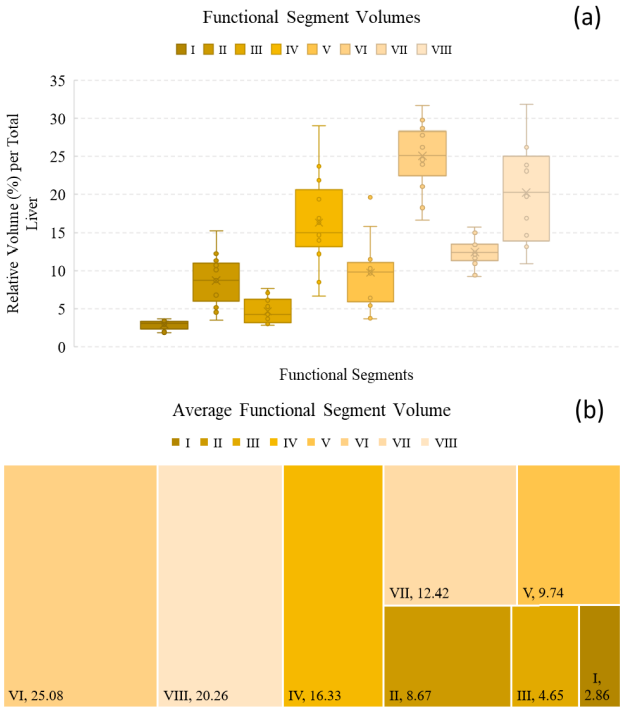


**FIGURE 9.** Box-Whisker (a) and tree plots (b) of functional segments (I – VIII) volumes and their averages, respectively.

to individual whole liver volume and corresponding averages are presented here. It can be noted from the table that, segment VI covered large portion of posterior section and has the most volumes (25.08%), while segment I was the smallest (2.86%).

Furthermore, besides the shape of exterior surface, hepatic venous networks played an equally important role in defining and localizing these segments. Accordingly, there existed noticeable cross-subject variability in the resulted resections. Especially, thanks to distributed vascular branches, the segment VIII exhibited the highest variability (6.5%), followed by segment IV (6.3%), whereas segment I did the lowest (0.6%).

An example of these variations is demonstrated in Fig. 10, where segment VIII was compared between subjects 10 (top) and 12 (bottom). It is clear that segment VIII in the former case was about one third (31.9%), while that in the latter one was only one tenth (10.9%), of the respective whole liver volume.

### 2) BENCHMARKING

To compare the proposed liver resection methods with recent related works, we performed relative volume evaluation, at three detail levels, i.e., lobes (left and right), sections (lateral, medial, anterior, and posterior), and functional segments (I-VIII), respectively. The benchmarking was made among Huang [17], Rusko [27], Cheng [20], Butdee [24] *et al.*, and our methods. Unfortunately, in [17], where venous tree was projected onto a plane, by which these liver segments were separated, segment I was thus missed out due to occlusion. Likewise, despite high degree of user interaction involved,

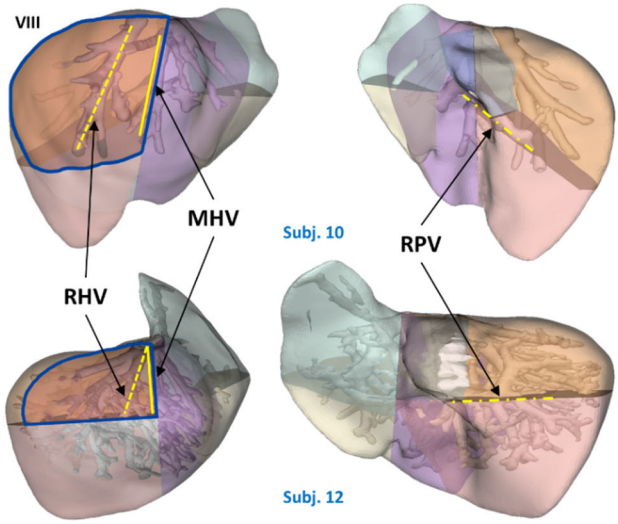


**FIGURE 10.** An example illustrating inter-subject functional segments variation between two subjects (top and bottom). Segment VIII, bounded by MHV, RHV, and RPV (solid, dashed, and dash-dotted yellow lines), was drawn on a respective liver surface (solid blue lines).

in [27], this segmented was merged with segment IV. In Cheng *et al.*'s work [20], only portal vein was considered, inflow and outflow blood to and from each segment was not guaranteed. Finally, segment I was explicitly estimated by Bézier curves, which required experienced judgment from an operator, unlike ours where the automated process relied on extracted anatomical landmarks. Since different labeling schemes were presented in those works, we decided to follow the most closely related one [27] and compared segments I and IV in merging, in the following analyses.

### 3) EVALUATION AT LOBE-LEVEL

Fig. 11 compares the averaged lobe volumes on both side among different methods. It is evident that, regardless of the methods used, the right hemi-liver was always larger than the left one. Particularly, our results were most similar to those by Rusko *et al.*, i.e., left: right volumes of 67.50: 32.50. This was not only because we analyzed the same dataset, but these findings also implied that the proposed resection yielded results, that were closely resemble to those obtained by that intervened by an experienced operator.

### 4) EVALUATION AT SECTION-LEVEL

Table 4 presents averaged proportions of volume sizes in 4 sections, i.e., lateral, medial, anterior, and posterior. It can be noted that our segmentations concurred with Butdee's for anterior section (30.0 vs. 29.4%) and with Rusko's for both lateral (13.3 vs 12.2%) and medial (19.2 vs. 20.0) sections.

To gain better insights into differential characteristics, PCA was applied to these relative volumes (by column) over these methods (by row). Their respective projections onto the principal 2D (eigen) space are plotted in Fig. 12. It is evident from the figure that, our method yielded similar sectional proportions to the semi-automatic methods [24], [27] (dotted arrows), within $2.0\sigma$ radius. It is also worth emphasizing

**TABLE 3.** Percentage of functional segment volumes, with respec to that of an individual whole liver.

| Subject | Seg I | Seg II | Seg III | Seg IV | Seg V | Seg VI | Seg VII | Seg VIII |
|---|---|---|---|---|---|---|---|---|
| 1 | 3.2% | 10.7% | 3.3% | 19.4% | 10.5% | 18.2% | 10.9% | 23.9% |
| 2 | 3.0% | 7.2% | 3.0% | 16.9% | 10.3% | 24.4% | 12.2% | 23.2% |
| 3 | 3.5% | 15.2% | 6.1% | 29.0% | 5.4% | 16.7% | 9.4% | 14.6% |
| 4 | 3.0% | 11.3% | 5.3% | 23.7% | 9.8% | 24.6% | 9.2% | 13.1% |
| 5 | 3.6% | 10.1% | 3.6% | 8.5% | 19.6% | 29.8% | 11.6% | 13.2% |
| 6 | 1.9% | 6.9% | 3.0% | 6.7% | 10.6% | 28.7% | 15.7% | 26.5% |
| 7 | 3.2% | 4.5% | 3.6% | 14.7% | 15.8% | 27.8% | 13.5% | 16.9% |
| 8 | 3.2% | 10.3% | 7.1% | 14.0% | 6.4% | 23.9% | 12.1% | 23.1% |
| 9 | 2.4% | 5.1% | 4.2% | 12.2% | 9.7% | 31.7% | 14.9% | 19.7% |
| 10 | 1.8% | 3.5% | 2.7% | 21.9% | 3.7% | 21.1% | 13.4% | *31.9%* |
| 11 | 2.1% | 6.8% | 7.6% | 14.1% | 3.7% | 26.2% | 13.4% | 26.2% |
| 12 | 3.4% | 12.3% | 6.3% | 15.0% | 11.5% | 28.0% | 12.7% | *10.9%* |
| *Average* | ***2.86%*** | *8.67%* | *4.65%* | *16.33%* | *9.74%* | ***25.08%*** | *12.42%* | *20.26%* |
| *Standard Deviation* | *0.6%* | *3.5%* | *1.7%* | *6.3%* | *4.7%* | *4.6%* | *2.0%* | ***6.5%*** |

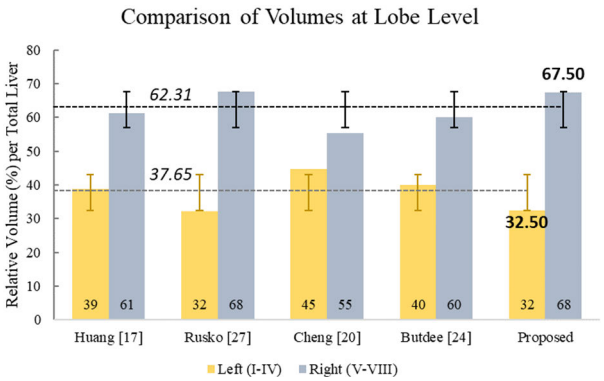


**FIGURE 11.** Comparisons of relative segment volumes at lobe-level. Our results closely resembled to those obtained by Rusko's method. Dotted lines are the average volumes of left and right lobes, for all methods.

**TABLE 4.** Averaged proportions (in %) of volume sizes in four sections, i.e., lateral, medial, anterior, and posterior.

| Methods | Lateral | Medial | Anterior | Posterior |
|---|---|---|---|---|
| Huang | 14.1 | 24.7 | 39.3 | 21.9 |
| Rusko | **12.2** | **20.0** | 40.2 | 27.6 |
| Cheng | 26.7 | 18.1 | 23.3 | 32.0 |
| Butdee | 17.9 | 22.1 | **29.4** | 30.6 |
| Proposed | 13.3 | 19.2 | 30.0 | 37.5 |

here that, in this analysis, section I was merged with IV, and associated with medial section.

### 5) EVALUATION AT FUNCTIONAL SECTION-LEVEL

Similar to the previous level, Table 5 presents the averaged proportions of volume sizes in all functional segments.

The above results indicated that our results were most consistent with Butdee's, for four out of seven segments, i.e., II, V, VI, and VII. This is mainly because we took the same approach in constructing the HV plane.

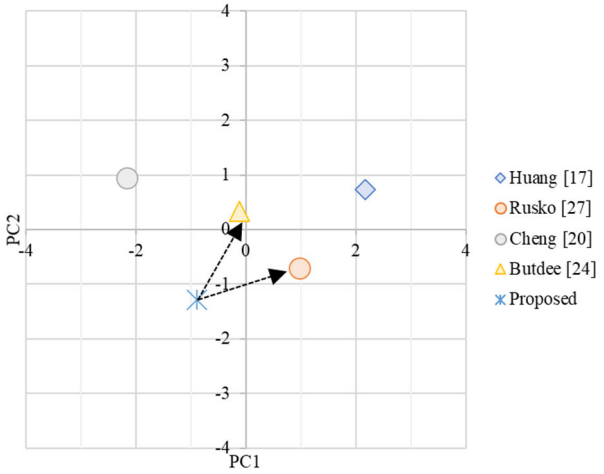


**FIGURE 12.** The distributions of volume sizes evaluated at section level by five methods and projected onto a 2D principal plane.

**TABLE 5.** Averaged proportions (in %) of volume sizes in seven functional segments, i.e., II, III, I & IV, and V – VIII.

| Methods | II | III | I, IV | V | VI | VII | VII |
|---|---|---|---|---|---|---|---|
| Huang | 3.0 | 11.1 | 24.7 | 20.6 | 6.1 | 15.8 | 18.7 |
| Rusko | 5.9 | 6.3 | **20.0** | 16.2 | 10.6 | 16.8 | 24.0 |
| Cheng | **8.4** | 18.2 | 18.1 | 6.3 | 15.6 | 16.4 | 16.9 |
| Butdee | 13.1 | **4.8** | 22.1 | **11.4** | **18.6** | **12.0** | 18.0 |
| Proposed | 8.7 | 4.6 | 19.2 | 9.7 | 25.1 | 12.4 | 20.3 |

For segments II, I & IV, and VIII, our results were comparable to those by Cheng, Rusko, and Huang *et al.*'s works, respectively. Likewise, these are because for these segments we referred to the similar markers as did those works.

PCA was also applied to these relational data, similar to those evaluated at the section-level, and the corresponding projections are plotted in Fig. 13, where individual subjects,

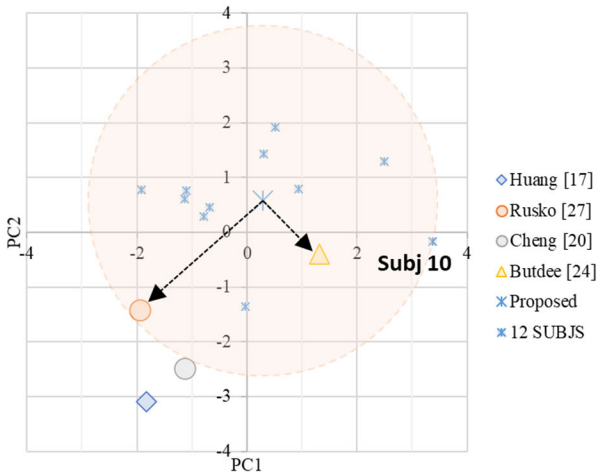


**FIGURE 13.** The distributions of volume sizes evaluated at segment level by five methods and projected onto a 2D principal plane. The projections of individual samples analyzed by our method are included.

analyzed by our method are also shown. Contradicted segment is manifest in partial deviation from its general cluster.

Unlike Fig. 12, however, due to higher dimension (8) than methods (5), PCA was applied to all 12 subjects and averages of compared methods ($12 + 4 = 16 > 8$). Based on Mahalanobis's distance, all instances but Huang's average, lied within $2.4\sigma$ radius (bounded by subject 10) around our average. Apart from that, our sample average was closest to Butdee's ($d = 1.0\sigma$), followed by Rukso's ($2.1\sigma$), and Cheng's ($2.4\sigma$). Despite similar volumes ratios, the proposed method outperformed these semi-automatic ones, especially in terms of the extent of user interaction and expertise involved, and hence inter- and intra-observer variability [7]. Take Rukso's method, for instance, between three trial runs, the volume variations ranged 2.8–5.6%, which is roughly at similar significance levels as those among five methods, presented in Table 5.

In addition to state-of-the-art methods, a range of computer software has also been developed based on Couinaud's definition. They are widely applied in clinical practice and worth mentioned here [59], e.g., MeVis LiverAnalyzer$^{TM}$(MeVis Medical Solution, Germany), and Synapse Vincent$^{TM}$(Fujifilm, Japan), etc. While the former requires its user to submit CT images and then wait for full report, the latter is interactive and thus depends greatly on user's expertise, e.g., significant manual adjustment is required for regions with poor vascular clearance, etc. Therefore, to resolve these limitations, algorithmic enhancement has still remained vital and been an active area of research [18], [20], [21], [24], [25], [28].

## VI. CONCLUSION

This paper presented a novel scheme for labeling functional segments of a liver mass and tracing on its surface virtual surgical paths for preoperative liver resection. This scheme took into account liver morphology, its interior vascular network, and anatomical landmarks. Given a liver and its vascular surfaces extracted from 3D CT, we divided a liver into eight functional segments, according to Couinaud's definition. Among key hepatic markers, our method was able to identify and localize gallbladder fossa and falciform ligaments on the liver surface, by means of differential geometry operations. Unlike existing methods, these and other markers considered herein were practical and much faithful to hepatic anatomy than manually specified cutting planes or curves. Besides only a few markers being placed by a user on major vessels, the rest of our process was automatic. Accordingly, this significantly reduced observer variability, user fatigue, and needs of radiological expertise.

To the best of our knowledge, existing schemes estimated the caudate lobe (segment I), based primarily on a portal vein or manually drawn parametric curves, or more often than not neglected this segment all together. To resolve this issue, the proposed method meticulously defined caudate boundaries based on surrounding segments and local planes. Particularly the extracted gallbladder fossa and falciform ligament forms natural landmarks that enabled its separation from lateral, medial, and right sections. Moreover, the principal vectors approximating main HV and PV branches ensured necessary blood passages in and out of each segment.

To demonstrate its merits, the proposed scheme was validated both visually and numerically on standard public liver dataset, called SLIVER07. A Total of twelve subjects were undergone virtual preoperative resection. The resulted functional segments were subsequently validated and benchmarked against four related methods. Numerical evaluations at three volumetric levels were performed and discussed.

One of our main contributions was well motivated by a previous work presented in [22], where gallbladder fossa and falciform ligament were both considered. However, with our work, the structures of interest were automatically identified, by optimizing parametric curvatures, based on their two-manifold distribution. Another key contribution was that, in addition to referring to these structures and the centroid of liver mass, our method also detected and analyzed its vasculature and other salient anatomical markers, in building resection planes. Unfortunately, numerical measurements were not reported in [22], we were thus unable to compare ours results with theirs. That said, our methods corresponded well to other counterparts, particularly to those depending on fair amount of interaction from an experienced user.

To summarize, successful liver resection procedure is characterized by accurate calculation of postoperative FLRV and functional independence of affected regions. Thus, it is anticipated that the proposed virtual resection method will benefit both preoperative planning and surgical intervention. Future directions worth considered are much precise extraction of vessels and their centerlines [21], [30] and building statistical atlas [39] of functional segments model. Empirical results reported herein have also confirmed large variations of vascular structures (especially HVs) [60] and related segments. It is thus worth further explore and correlate these resections with, for examples, biliary tree, by using

CT-MRCP (MR cholangiopancreatography) perfusion and functional parenchyma, by using particular contrast material.

## ACKNOWLEDGMENT

The authors would like to thank T. Heimann, B. van Ginneken, M. Styner, and G. Humpire for organizing and hosting MICCAI SLIVER07 dataset, employed in this study.

## REFERENCES

[1] Y. Kishi, E. K. Abdalla, Y. S. Chun, D. Zorzi, D. C. Madoff, M. J. Wallace, S. A. Curley, and J. N. Vauthey, "Three hundred and one consecutive extended right hepatectomies: Evaluation of outcome based on systematic liver volumetry," *Ann. Surg.*, vol. 250, pp. 540–548, Oct. 2009.

[2] E. K. Abdalla, C. C. Barnett, D. Doherty, S. A. Curley, and J. N. Vauthey, "Extended hepatectomy in patients with hepatobiliary malignancies with and without preoperative portal vein embolization," *Arch. Surg.*, vol. 137, pp. 675–680, Jun. 2002.

[3] M. Ben-Haim, S. Emre, T. M. Fishbein, P. A. Sheiner, C. A. Bodian, L. Kim-Schluger, M. E. Schwartz, and C. M. Miller, "Critical graft size in adult-to-adult living donor liver transplantation: Impact of the recipient's disease," *Liver Transplantation*, vol. 7, no. 11, pp. 948–953, Nov. 2001.

[4] A. Akdur, M. Kirnap, F. Ozcay, A. Sezgin, H. E. A. Soy, F. K. Yarbug, S. Yildirim, G. Moray, G. Arslan, and M. Haberal, "Large-for-size liver transplant: A single-center experience," *Express Clin. Transpl.*, vol. 13, pp. 108–110, Apr. 2015.

[5] M.-A. Allard, F. Lopes, F. Frosio, N. Golse, A. Sa Cunha, D. Cherqui, D. Castaing, R. Adam, and E. Vibert, "Extreme large-for-size syndrome after adult liver transplantation: A model for predicting a potentially lethal complication," *Liver Transplantation*, vol. 23, no. 10, pp. 1294–1304, Oct. 2017.

[6] M. C. Lim, C. H. Tan, J. Cai, J. Zheng, and A. W. C. Kow, "CT volumetry of the liver: Where does it stand in clinical practice?" *Clin. Radiol.*, vol. 69, no. 9, pp. 887–895, Sep. 2014.

[7] J. Keegan, P. Horkaew, T. J. Buchanan, T. S. Smart, G.-Z. Yang, and D. N. Firmin, "Intra- and interstudy reproducibility of coronary artery diameter measurements in magnetic resonance coronary angiography," *J. Magn. Reson. Imag.*, vol. 20, no. 1, pp. 160–166, Jul. 2004.

[8] K. Vekemans and F. Braet, "Structural and functional aspects of the liver and liver sinusoidal cells in relation to colon carcinoma metastasis," *World J. Gastr.*, vol. 11, no. 33, pp. 5095–5102, Sep. 2005.

[9] C. Couinaud, "Liver anatomy: Portal (and suprahepatic) or biliary segmentation," *Dig. Surg.*, vol. 16, no. 6, pp. 459–467, 1999.

[10] Y. W. J. Jones. *Couinaud Classification of Hepatic Segments*. Accessed: Nov. 20, 2020. [Online]. Available: https://radiopaedia.org/articles/couinaud-classification-of-hepatic-segments?lang=us

[11] M. F. Chen, T. L. Hwang, and C. F. Hung, "Human liver regeneration after major hepatectomy. A study of liver volume by computed tomography," *Ann. Surg.*, vol. 213, no. 3, pp. 227–229, Mar. 1991.

[12] W. Lamade, G. Glombitza, L. Fischer, P. Chiu, C. E. Cárdenas, M. Thorn, H. P. Meinzer, L. Grenacher, H. Bauer, T. Lehnert, and C. Herfarth, "The impact of 3-dimensional reconstructions on operation planning in liver surgery," *Arch. Surg.*, vol. 135, no. 11, pp. 1256–1261, Nov. 2000.

[13] B. Reitinger, A. Bornik, R. Beichel, and D. Schmalstieg, "Liver surgery planning using virtual reality," *IEEE Comput. Graph. Appl.*, vol. 26, no. 6, pp. 36–47, Nov./Dec. 2006.

[14] Y. Oshiro and N. Ohkohchi, "Three-dimensional liver surgery simulation: Computer-assisted surgical planning with three-dimensional simulation software and three-dimensional printing," *Tissue Eng. A*, vol. 23, nos. 11–12, pp. 474–480, Jun. 2017.

[15] C. T. Yeo, A. MacDonald, T. Ungi, A. Lasso, D. Jalink, B. Zevin, G. Fichtinger, and S. Nanji, "Utility of 3D reconstruction of 2D liver computed tomography/magnetic resonance images as a surgical planning tool for residents in liver resection surgery," *J. Surgical Edu.*, vol. 75, no. 3, pp. 792–797, May 2018.

[16] D. Selle, B. Preim, A. Schenk, and H.-O. Peitgen, "Analysis of vasculature for liver surgical planning," *IEEE Trans. Med. Imag.*, vol. 21, no. 11, pp. 1344–1357, Nov. 2002.

[17] S. H. Huang, B.-L. Wang, M. Cheng, W.-L. Wu, X.-Y. Huang, and Y. Ju, "A fast method to segment the liver according to Couinaud's classification," in *Medical Imaging and Informatics*, X. Gao, H. Müller, M. J. Loomes, R. Comley, and S. Luo, Eds. Berlin, Germany: Springer, 2008, pp. 270–276.

[18] X. Yang, J. D. Yang, H. P. Hwang, H. C. Yu, S. Ahn, B.-W. Kim, and H. You, "Segmentation of liver and vessels from CT images and classification of liver segments for preoperative liver surgical planning in living donor liver transplantation," *Comput. Methods Programs Biomed.*, vol. 158, pp. 41–52, May 2018.

[19] H. G. Debarba, D. J. Zanchet, D. Fracaro, A. Maciel, and A. N. Kalil, "Efficient liver surgery planning in 3D based on functional segment classification and volumetric information," in *Proc. Annu. Int. Conf. IEEE Eng. Med. Biol.*, Aug. 2010, pp. 4797–4800.

[20] Y. Chen, X. Yue, C. Zhong, and G. Wang, "Functional region annotation of liver CT image based on vascular tree," *Biomed. Res. Int.*, vol. 2016, Jan. 2016, Art. no. 5428737.

[21] Q. Zhang, Y. Fan, J. Wan, and Y. Liu, "An efficient and clinical-oriented 3D liver segmentation method," *IEEE Access*, vol. 5, pp. 18737–18744, 2017.

[22] D. Boltcheva, N. Passat, V. Agnus, M. A. J.-D. Col, C. Ronse, and L. Soler, "Automatic anatomical segmentation of the liver by separation planes," *Proc. SPIE*, vol. 6141, Jan. 2006, Art. no. 61411A.

[23] D. Oliveira, R. Feitosa, and M. Correia, "Automatic Couinaud liver and veins segmentation from CT images," in *Proc. Int. Conf. Biomed. Elect. Dev.*, 2008, pp. 249–252.

[24] C. Butdee, C. Pluempitiwiriyawej, and N. Tanpowpong, "3D plane cuts and cubic Bézier curve for CT liver volume segmentation according to Couinaud's classification," *Songk. J. Sci. Tech.*, vol. 39, pp. 793–801, Nov./Dec. 2017.

[25] M.-A. Lebre, A. Vacavant, M. Grand-Brochier, H. Rositi, A. Abergel, P. Chabrot, and B. Magnin, "Automatic segmentation methods for liver and hepatic vessels from CT and MRI volumes, applied to the couinaud scheme," *Comput. Biol. Med.*, vol. 110, pp. 42–51, Jul. 2019.

[26] V. Pamulapati, A. Venkatesan, B. Wood, and M. G. Linguraru, "Liver segmental anatomy and analysis from vessel and tumor segmentation via optimized graph cuts," in *Proc. ABD-MICCAI*, 2011, pp. 189–197.

[27] L. Ruskó, I. Mátéka, and A. Kriston, "Virtual volume resection using multi-resolution triangular representation of B-spline surfaces," *Comput. Methods Programs Biomed.*, vol. 111, no. 2, pp. 315–329, Aug. 2013.

[28] O. I. Alirr and A. A. A. Rahni, "Automatic atlas-based liver segmental anatomy identification for hepatic surgical planning," *Int. J. Comput. Assist. Radiol. Surg.*, vol. 15, no. 2, pp. 239–248, Feb. 2020.

[29] M. Moghbel, S. Mashohor, R. Mahmud, and M. I. B. Saripan, "Review of liver segmentation and computer assisted detection/diagnosis methods in computed tomography," *Artif. Intell. Rev.*, vol. 50, no. 4, pp. 497–537, Dec. 2018.

[30] S. Moccia, E. D. Momi, S. El Hadji, and L. S. Mattos, "Blood vessel segmentation algorithms—Review of methods, datasets and evaluation metrics," *Comput. Methods Programs Biomed.*, vol. 158, pp. 71–91, May 2018.

[31] Y. Li, G. Wang, M. Li, J. Li, L. Shi, and J. Li, "Application of CT images in the diagnosis of lung cancer based on finite mixed model," *Saudi J. Biol. Sci.*, vol. 27, no. 4, pp. 1073–1079, Apr. 2020.

[32] A. Rosenfeld, R. A. Hummel, and S. W. Zucker, "Scene labeling by relaxation operations," *IEEE Trans. Syst., Man, Cybern.*, vol. SMC-6, no. 6, pp. 420–433, Jun. 1976.

[33] Y. Boykov and V. Kolmogorov, "An experimental comparison of min-cut/max-flow algorithms for energy minimization in vision," *IEEE Trans. Pat. Anal. Mach. Intell.*, vol. 26, no. 9, pp. 1124–1137, Sep. 2004.

[34] W. E. Lorensen and H. E. Cline, "Marching cubes: A high resolution 3D surface construction algorithm," *ACM SIGGRAPH Comput. Graph.*, vol. 21, no. 4, pp. 163–169, Aug. 1987.

[35] L. Antiga, "Patient-specific modeling of geometry and blood flow in large arteries," Ph.D. dissertation, Dept. Bioeng., Politechico di Milano, Milan, Italy, 2002.

[36] D. J. Bartholomew, "Principal components analysis," in *International Encyclopedia of Education*, P. Peterson, E. Baker, and B. McGaw, Eds. 3rd ed. Oxford, U.K.: Elsevier, 2010, pp. 374–377.

[37] M. Meyer, M. Desbrun, P. Schröder, and A. H. Barr, "Discrete differential-geometry operators for triangulated 2-manifolds," in *Visualization and Mathematics III*, H. C. Hege and K. Polthier, Eds. Berlin, Germany: Springer, 2003, pp. 35–57.

[38] H. Zhao and G. Xu, "Triangular surface mesh fairing via Gaussian curvature flow," *J. Comput. Appl. Math.*, vol. 195, nos. 1–2, pp. 300–311, Oct. 2006.
[39] P. Horkaew and G. Z. Yang, "Construction of 3D dynamic statistical deformable models for complex topological shapes," in *Proc. MICCAI Conf.*, in Lecture Notes in Computer Science, vol. 3216. Berlin, Germany: Springer, 2004, pp. 217–224.
[40] E. Magid, O. Soldea, and E. Rivlin, "A comparison of Gaussian and mean curvature estimation methods on triangular meshes of range image data," *Comput. Vis. Image Understand.*, vol. 107, no. 3, pp. 139–159, Sep. 2007.
[41] M. Zhihong, C. Guo, M. Yanzhao, and K. Lee, "Curvature estimation for meshes based on vertex normal triangles," *Comput.-Aided Des.*, vol. 43, no. 12, pp. 1561–1566, Dec. 2011.
[42] M. M. Mesmoudi, L. D. Floriani, and P. Magillo, "Discrete curvature estimation methods for triangulated surfaces," in *Applications of Discrete Geometry and Mathematical Morphology*, U. Köthe, A. Montanvert, and P. Soille, Eds. Berlin, Germany: Springer, 2012, pp. 28–42.
[43] H. Huang, S. Wu, D. Cohen-Or, M. Gong, H. Zhang, G. Li, and B. Chen, "L1-medial skeleton of point cloud," *ACM Trans. Graph.*, vol. 32, no. 4, pp. 65:1–65:8, 2013.
[44] W. Stehr and C. A. Gingalewski, "Other causes of intestinal obstruction," in *Pediatric Surgery*, A. G. Coran Ed., 7th ed. Philadelphia, PA, USA: Mosby, 2012, ch. 87, pp. 1127–1134.
[45] V. Garbar and B. W. Newton, *Anatomy, Abdomen and Pelvis, Falciform Ligament*. Treasure Island, FL, USA: StatPearls Publishing, 2020. Accessed: Nov. 1, 2020. [Online]. Available: http://www.ncbi.nlm.nih.gov/books/NBK539858
[46] M. Kumon, "Anatomical study of the caudate lobe with special reference to portal venous and biliary branches using corrosion liver casts and clinical application," *Liver Cancer*, vol. 6, no. 2, pp. 161–170, 2017.
[47] M. A. Wahab, O. Fathy, E. Elhanafy, E. Atif, A. M. Sultan, T. Salah, M. Elshoubary, N. Anwar, and A. Sultan, "Caudate lobe resection for hepatocellular carcinoma," *Hepatogastroenterology*, vol. 58, no. 112, pp. 1904–1908, Oct. 2011.
[48] M. G. Sagoo, R. C. Aland, and E. Gosden, "Morphology and morphometry of the caudate lobe of the liver in two populations," *Anatomical Sci. Int.*, vol. 93, no. 1, pp. 48–57, Jan. 2018.
[49] B. M. Brown, R. A. Filly, and P. W. Callen, "Ultrasonographic anatomy of the caudate lobe," *J. Ultrasound Med.*, vol. 1, no. 5, pp. 189–192, Jun. 1982.
[50] C. Gang, L. Xuecheng, W. Guoqing, Y. Rigao, Z. Shaoxiang, T. Liwen, and D. Jiahong, "Sectional anatomy of the caudate lobe of liver: Based on coronal and sagittal sections," *J. Med. Colleges PLA*, vol. 24, no. 4, pp. 187–197, Aug. 2009.
[51] T. Heimann *et al.*, "Comparison and evaluation of methods for liver segmentation from CT datasets," *IEEE Trans. Med. Imag.*, vol. 28, no. 8, pp. 1251–1265, Aug. 2009.
[52] L. Soler, A. Hostettler, V. Agnus, A. Charnoz, J. Fasquel, J. Moreau, A. Osswald, M. Bouhadjar, and J. Marescaux, "3D image reconstruction for comparison of algorithm database: A patient specific anatomical and medical image database," IRCAD, Strasbourg, France, Tech. Rep., 2010. Accessed: Dec. 31, 2020. [Online]. Available: https://www.ircad.fr/research/3d-ircadb-01/
[53] *Vascular Modeling Toolkit*. Accessed: Oct. 20, 2020. [Online]. Available: http://www.vmtk.org/
[54] *Vascular Modeling Toolkit*. Accessed: Oct. 20, 2020. [Online]. Available: http://www.vmtk.org/, Accessed on: Oct. 20. 2020.
[55] R. Loffroy, S. Favelier, O. Chevallier, L. Estivalet, P.-Y. Genson, P. Pottecher, S. Gehin, D. Krausé, and J.-P. Cercueil, "Preoperative portal vein embolization in liver cancer: Indications, techniques and outcomes," *Quantum Imag. Med. Surg.*, vol. 5, no. 5, pp. 730–739, Oct. 2015.
[56] P.-A. Clavien, H. Petrowsky, M. L. DeOliveira, and R. Graf, "Strategies for safer liver surgery and partial liver transplantation," *New England J. Med.*, vol. 356, no. 15, pp. 1545–1559, Apr. 2007.
[57] S. Breitenstein, C. Apestegui, H. Petrowsky, and P. A. Clavien, "State of the art in liver resection and living donor liver transplantation: A worldwide survey of 100 liver centers," *World J. Surg.*, vol. 33, no. 4, pp. 797–803, Apr. 2009.
[58] F. Vandenbroucke-Menu, A. Gotra, L. Sivakumaran, G. Chartrand, K.-N. Vu, C. Kauffmann, S. Kadoury, B. Gallix, J. A. D. Guise, and A. Tang, "Liver segmentation: Indications, techniques and future directions," *Insights Imag.*, vol. 8, no. 4, pp. 377–392, Aug. 2017.
[59] M. Shimoda, M. Hariyama, Y. Oshiro, and S. Suzuki, "Development of new software enabling automatic identification of the optimal anatomical liver resectable region, incorporating preoperative liver function," *Oncol. Lett.*, vol. 18, pp. 6639–6647, Oct. 2019.
[60] C.-H. Fang, J.-H. You, W. Y. Lau, E. C. H. Lai, Y.-F. Fan, S.-Z. Zhong, K.-X. Li, Z.-X. Chen, Z.-H. Su, and S.-S. Bao, "Anatomical variations of hepatic veins: Three-dimensional computed tomography scans of 200 subjects," *World J. Surg.*, vol. 36, no. 1, pp. 120–124, Jan. 2012.

**DOAN CONG LE** received the M.S. degree in computer science from the Vietnam National University Ho Chi Minh City–University of Science (VNUHCM-US), in 2014. He is currently pursuing the Ph.D. degree with the School of Computer Engineering, Suranaree University of Technology, Thailand. His research interests include image segmentation and 3D face reconstruction.

**JIRAPA CHANSANGRAT** received the M.D. degree (Hons.) from the Siriraj Hospital, Mahidol University, Thailand, in 2010. Her research interests include diagnostic radiology, vascular imaging, doppler ultrasound, interventional oncology, and interventional radiology. She is currently a member of the Medical Association of Thailand, the Royal College of Radiologist of Thailand, the Thai Resuscitation Council, and the Thai Society of Vascular and Interventional Radiology. She received the Residence Training in Diagnostic Radiology in 2016 and the Fellowship of Body Interventional Radiology in 2020. She also received many prestigious certificates and awards, e.g., Radiologic-Pathology Correlation, Seattle, WA, USA, in 2015, the Diploma of the Thai Board of Diagnostic Radiology, Thailand, in 2016, and the Certification of Body Interventional Radiology in 2020.

**NATTAWUT KEERATIBHARAT** received the M.D. degree from Srinakharinwirot University, Thailand, in 2010. His research interests include minimally invasive surgery, liver and biliary surgery, pancreatic surgery, colorectal surgery, image guided surgery, and endoscopy. He is currently a member of the Medical Association of Thailand, the Royal College of Surgeons of Thailand, and the International College of Surgeons, Thailand. He received Residence Training in General Surgery in 2017. He was a Fellowship in Colorectal Surgery in 2018, the Seoul St. Mary Hospital, Catholic University of Korea, Republic of Korea. He also received many prestigious certificates, e.g., the Advanced Trauma Life Support, Royal College Surgeons of Thailand, in 2011, and the Diploma of the Thai Board of General Surgery, Thailand, in 2017.

**PARAMATE HORKAEW** received the B.Eng. degree (Hons.) in telecommunication engineering from the King Mongkut's Institute of Technology, Ladkrabang, Thailand, in 1999, and the Ph.D. degree in computer science from Imperial College London, U.K., in 2004. He is currently an Assistant Professor with the School of Computer Engineering, Suranaree University of Technology, Thailand. His research interests include medical image analysis, computer aided diagnosis and surgery, computational anatomy, digital geometry processing, and computer vision.